Thallium isotopes reveal protracted anoxia associated with volcanism, carbon burial, and mass extinction during the Toarcian (Early Jurassic)

Theodore R. Them II[a1], Benjamin C. Gill[b], Andrew H. Caruthers[c], Angela M. Gerhardt[b,d], Darren R. Gröcke[e], Timothy W. Lyons[f], Selva M. Marroquín[b], Sune G. Nielsen[g], João P. Trabucho Alexandre, and Jeremy D. Owens[a]

[a]*Department of Earth, Ocean and Atmospheric Science & National High Magnetic Field Laboratory, Florida State University, Tallahassee, Florida 32306, USA*

[b]*Department of Geosciences, Virginia Polytechnic Institute and State University, Blacksburg, Virginia 24061, USA*

[c]*Department of Geosciences, Western Michigan University, Kalamazoo, Michigan 49006, USA*

[d]*Enervest, Ltd, Houston, Texas 77002, USA*

[e]*Department of Earth Sciences, Durham University, Durham, DH1 3LE, UK*

[f]*Department of Earth Sciences, University of California, Riverside, California 92521 USA*

[g]*Department of Geology and Geophysics, Woods Hole Oceanographic Institution, Woods Hole, Massachusetts 02543, USA*

[h]*Department of Earth Sciences, Universiteit Utrecht, P. O. Box 80115 3508 TC Utrecht, The Netherlands*

[1]Corresponding author: tthem@fsu.edu

PHYSICAL SCIENCES: Earth, Atmospheric, and Planetary Sciences

For this study, we generated thallium (Tl) isotope records from two anoxic basins to track the earliest changes in global bottom water oxygen contents over the Toarcian Oceanic Anoxic Event (T-OAE) of the Early Jurassic (~183 Ma). The T-OAE, like other Mesozoic OAEs, has been interpreted as an expansion of marine oxygen depletion based on indirect methods such as organic-rich facies, carbon isotope excursions, and biological turnover. Our Tl isotope data, however, reveal explicit evidence for earlier global marine deoxygenation of ocean water, some 600 ka before the classically defined T-OAE. This antecedent deoxygenation occurs at the Pliensbachian/Toarcian boundary and is coeval with the onset of initial large igneous province (LIP) volcanism and the initiation of a marine mass extinction. Thallium isotopes are also perturbed during the T-OAE interval, as defined by carbon isotopes, reflecting a second deoxygenation event that coincides with the acme of elevated marine mass extinctions and the main phase of LIP volcanism. This suggests that the duration of widespread anoxic bottom waters was at least one million years in duration and spanned early to middle Toarcian time. Thus, the Tl data reveal a more nuanced record of marine oxygen depletion and its links to biological change during a period of climatic warming in Earth's past and highlights the role of oxygen depletion on past biological evolution.

Keywords: Toarcian Oceanic Anoxic Event; Early Jurassic; Thallium isotopes; carbon isotope excursion; large igneous province; mass extinction

Significance Statement

Declining oxygen contents in today's oceans highlight the need to better understand ancient, natural marine deoxygenation and associated extinctions. In the Early Jurassic, the Toarcian Oceanic Anoxic Event (T-OAE; ~183 Ma) is associated with significant perturbations to the Earth system, historically defined by carbon isotopes. We reconstructed global oceanic (de)oxygenation using thallium isotopes from two ocean basins that suggest a stepwise decline of oxygen that initiated before and extended well after the classically defined T-OAE interval. This initial deoxygenation occurs with the start of massive volcanism and marine extinctions while a later shift corresponds to the traditional T-OAE. This emphasizes the need for more nuanced records of ancient environmental and biogeochemical feedbacks that lead to and maintain widespread marine anoxia.

Introduction

The amount of oxygen dissolved in the modern ocean is decreasing (1, 2), due in part to the increasing concentration of greenhouse gases in the atmosphere. Similar scenarios have likely occurred throughout geologic history. For example, during transient intervals in the Mesozoic—known as oceanic anoxic events (or OAEs)—substantial increases in atmospheric greenhouse gases are linked to the volcanic emissions of large igneous provinces (LIPs); these changes are hypothesized as the primary driver of OAEs (3–5). Understanding the mechanisms underlying intervals of marine deoxygenation in Earth history, such as OAEs, is essential because they are intimately linked with ecological shifts and specifically marine mass extinctions (6). Additionally, they provide us with an analog for possible future changes in the long-term oxygen inventory of

92 the ocean of our planet (7, 8).

93 The concept of an OAE was proposed by ref. 9 to explain the multiple ocean basin
94 occurrences of coeval organic-matter-rich sediments, or black shales, deposited at a wide range of
95 water depths on the middle Cretaceous ocean floor. OAEs were defined as brief (<1 Ma) episodes
96 of expansion and intensification of the oxygen minimum layer in the ocean. This expanding layer
97 encroached on the seafloor of seamounts, submarine plateaus, and continental margins and resulted
98 in enhanced burial of organic matter in widespread black shales. The broad temporal association
99 of these black shales with positive excursions in the marine carbon isotope record was
100 subsequently documented (10). These excursions have been interpreted to reflect the elevated
101 burial of ^{13}C-depleted organic carbon during the OAE (e.g., 4, 5, 10–16). The concept of an OAE
102 was later applied to a positive excursion in the carbon isotope record of Tethyan Lower Jurassic
103 limestones during what is now known as the Toarcian OAE (15).

104 Subsequent studies of the Toarcian OAE identified an abrupt, large magnitude, negative
105 carbon isotope excursion (CIE) at ca. 183.1 Ma that interrupts a broader positive CIE noted by ref.
106 15. Generally, this negative CIE appears to define the onset of major environmental disruption,
107 the onset of organic-rich deposition, and the main pulse of mass extinction (5, 17–19) (Fig. 1). A
108 carbon isotope compilation of published work has also shown that the broader early Toarcian
109 positive CIE actually begins at the Pliensbachian/Toarcian boundary (Fig. 1, SI Fig. 3) (5, 20, 21).
110 However, this broader positive CIE precedes the onset of organic-rich deposition that defines the
111 start of the T-OAE at many locations (5, 16, and many others) (Fig. 1, SI Fig. 3, SI Text) (Fig. 1),
112 thus it has not been generally considered part of the T-OAE. This interval is also intriguing because
113 it corresponds to the beginning of a mass extinction that later reaches its climax during the T-OAE
114 (19).

Although positive CIEs could represent the effects of large-scale oxygen depletion in seawater, other environmental variables can contribute to the carbon isotope record (22, 23), and there is no simple relationship between redox conditions and organic matter preservation (24, as reviewed by ref. 25). Thus, the culmination of a positive CIE does not require global ocean deoxygenation or even increased organic carbon burial (22, 24–27), as carbon isotopes ultimately track the balance of all the input and output fluxes and associated isotope fractionations (22). For this reason, carbon isotope data cannot be used alone as a proxy for the expansion of oceanic anoxia. Additionally, evidence for decreasing marine oxygen inventories leading to OAEs is hampered since redox proxies typically constrain the most extreme euxinic (oxygen-free, sulfide-containing waters) end member (28–31). As such, uniquely constraining the global extent of non-sulfidic, anoxic waters has not been possible. This bias highlights the need for a more sensitive proxy that constrains more subtle changes in oceanic oxygen levels during OAEs and other oceanographic events in Earth history.

Using thallium isotopes to track global marine oxygen contents

Thallium isotopes in organic-matter-rich mudstones provide a novel window to secular variations in the oceanic oxygen inventory over the expanded T-OAE interval from the latest Pliensbachian to middle Toarcian (see Supplemental Information for Tl isotope nomenclature). The modern open ocean seawater Tl isotope composition (with a residence time of ca. 20 ka) is homogenous to within < 0.5 ε-units (32–34), and this seawater value is captured in the sediments deposited in euxinic settings (34). Thallium is introduced to the ocean by rivers, high-temperature hydrothermal fluids, volcanic emissions, mineral aerosols, and pore-water fluxes from continental-margin sediments. These sources have essentially identical Tl isotopic compositions of ε^{205}Tl ~-2

(as reviewed in ref. 35), which reflects minimal isotope fractionation during continental weathering and high-temperature mobilization of Tl. The major outputs of Tl from the marine system include adsorption onto manganese (Mn)-oxides and, low-temperature (<100°C) alteration of oceanic crust (AOC). Sedimentation of organic matter and sulfide minerals in low oxygen settings also removes Tl from seawater, but the global flux is relatively minor in the modern ocean (34, 36). Adsorption onto Mn-oxides and AOC are the only known processes that fractionate Tl.

Specifically, Mn oxides are heavier than seawater by ~+13-19 ε-units, which is likely due to equilibrium isotope fractionation during oxidation of univalent aqueous Tl to trivalent Tl when permanently sorbed to Mn oxides (35, 37, 38). The uncertainty associated with the Tl isotope fractionation factor during sorption to Mn oxides relates to Tl isotope variations found in some pelagic clays with somewhat less positive compositions (39). However, pure Mn oxides as found in Fe-Mn crusts display relatively constant offsets from seawater of ~+19±2 ε-units (32, 35), which is the preferred value for Tl isotope fractionation during sorption to Mn oxides.

The mechanism of Tl isotope fractionation during incorporation into AOC is less well understood but is likely a kinetic process whereby the light isotope is preferentially incorporated into AOC (35). Although individual samples of AOC can exhibit $\varepsilon^{205}Tl \sim -15$ (40) the average is more likely closer to $\varepsilon^{205}Tl \sim -7$ because uptake is close to quantitative from the circulating hydrothermal fluids (35), thus the fractionation from seawater is minimal.

Although the marine Tl residence time is long enough to produce a globally homogenous Tl isotope composition of the ocean it is still short enough that seawater $\varepsilon^{205}Tl$ can respond to rapid global changes in Mn-oxide burial on glacial-interglacial timescales (35; 41). In contrast, AOC deposition rates vary on extremely long timescales (>10^7 years) as it responds primarily to global average ocean crust production rates (42) and, hence, $\varepsilon^{205}Tl_{seawater}$ variations on timescales shorter

than ~1 million years are most likely driven by changes in Mn-oxide preservation and burial. Crucially, Mn-oxides are only buried in sediments with O_2 present at or near the sediment/water interface because they are rapidly dissolved under anoxic conditions (43). In turn, global Mn-oxide burial fluxes are related to the global extent of bottom water anoxia (34). As such, $\varepsilon^{205}Tl_{seawater}$ can be related to relative changes in oceanic oxygenation. Thallium isotopes have been applied to only one ancient climate perturbation that documents the global relationship between oceanic oxygenation leading up to the Cenomanian-Turonian event of OAE 2 (41), and it was shown that changes in carbon isotopes lagged the onset of marine deoxygenation, which underlines the potential for Tl isotopes to provide unique information about ancient oceanic oxygenation. During intervals of increased bottom water oxygen extent, $\varepsilon^{205}Tl_{seawater}$ values will be more negative, whereas during intervals of decreased bottom water oxygen extent (increase of bottom water anoxia), $\varepsilon^{205}Tl_{seawater}$ values will be more positive and approach their source value ($\varepsilon^{205}Tl$ = ~-2).

Study site selection

To reconstruct global ocean oxygen contents (or redox changes) using the Tl isotope system, it is necessary to constrain local water column redox conditions to be sure to capture the seawater value, thus avoiding any local Mn-oxide signatures. This is because variations in local sedimentary redox conditions and basinal restriction can influence the isotopic signals captured in the sedimentary record and can hamper the use of these records to reconstruct changes in global marine redox conditions (31, 36, 45, 46). Therefore, it is important to investigate multiple localities that were well-connected to the open ocean and have independent constraints on local redox conditions (e.g., 41, 47). Here, we analyzed samples from two Lower Jurassic successions that contain intervals that were deposited under euxinic conditions—as identified by established,

184 independent proxies for local redox, including Fe speciation—before, during, and after the T-OAE
185 (Fig. 2 and SI Figs. 1, 2). We first investigated three Pliensbachian and Toarcian sections of the
186 Fernie Formation from the Western Canada Sedimentary Basin, which represent deposition on an
187 open-ocean margin of northeastern Panthalassa (Fig. 2). These samples were taken from outcrop
188 (East Tributary) and two cores (1-35-62-20W5, 6-32-75-5W6). The other studied Toarcian
189 succession, Dotternhausen Quarry, Germany, represents deposition in a semi-restricted structural
190 basin in the European epeiric sea, which was connected to the Tethys Ocean (48) (Fig. 2).
191
192 **Results**
193 Data from the base of the East Tributary section, within the Pliensbachian portion of the
194 section (*Amaltheus margaritatus* ammonite Zone in Northwest Europe and *Fanninoceras kunae*
195 ammonite Zone in North America) start with a ε^{205}Tl of ~-6 (Fig. 3). These values are similar to
196 the ε^{205}Tl of modern seawater (34) and suggest a similar global Tl isotopic mass balance tied to
197 Mn-oxide burial and similar extents of oxygenated bottom waters. At the Pliensbachian/Toarcian
198 boundary, ε^{205}Tl gradually shifts to less negative values and remains steady until the onset of the
199 negative Toarcian CIE. We interpret this initial rise in ε^{205}Tl as the beginning of the expansion of
200 oceanic anoxia before the classically defined T-OAE (see Fig. 1) with a date of ~183.65 Ma (±
201 ~0.150 Ma) (49)—approximately 500–600 kyr before the onset of the negative CIE (50, 51) that
202 traditionally defines the base of the T-OAE. Furthermore, our δ^{13}C and ε^{205}Tl data from two drill
203 cores from elsewhere in the Western Canada Sedimentary Basin show similar values and trends
204 (see SI Figs 1 and 2), suggesting that they capture global signals and that Early Jurassic seawater
205 ε^{205}Tl values are also homogenous.
206 The German Dotternhausen Quarry section (31, 48), where the Pliensbachian/Toarcian

boundary is not present, shows time-equivalent ε^{205}Tl values (~-4) that are nearly identical, within analytical error, to results from Canada (~-3.5) for the lower Toarcian *Dactylioceras tenuicostatum* (equivalent) ammonite Zone (Fig. 3). The ε^{205}Tl values increase at the onset of the negative CIE, gradually decrease during the minimum of the CIE, and increase during the rising limb of the carbon isotope data (Fig. 3). A longer-term decrease of Tl isotopes occurs after the end of the negative CIE to the top of the section (Fig. 3). The similarities among all the study sites support the interpretation that these Tl isotope records represent primary global ocean signals, even in the more restricted setting of the German section.

Discussion

The shift in Tl isotopes from -6 to -4, as observed at the Pliensbachian/Toarcian boundary (Fig. 3), based on isotope mass balance calculations, requires a ~50 % decrease in the global burial of Mn-oxides (34). In all likelihood, the decline in marine Mn-oxide burial was linked to an expansion of bottom water anoxia, which restricted the area of oxic sediment deposition. This initial deoxygenation is notable because it generally coincides with 1) the interpreted onset of Karoo-Ferrar LIP activity (52, 53) at the start of the longer-term positive CIE, 3) initiation of a radiogenic osmium isotope excursion (49, 54), and 4) the beginning of a major marine extinction event (beginning of Phase 3 of ref. 19) (Fig. 4). These observations are consistent with marine deoxygenation caused by an increase in organic carbon export linked to enhanced chemical weathering and nutrient input to the oceans. This sequence led to increased oxygen consumption in the aphotic zone—driving the expansion of oxygen minima in the ocean that is recorded by Tl isotopes. The $^{187}Os/^{188}Os_i$ values decline soon after the Pliensbachian/Toarcian boundary (49, 54), suggesting that the rate of continental weathering declined. Thus, the sustained deoxygenation and

230 elevated organic carbon burial (Figs. 3 and 4), evidenced by the thallium and carbon isotope
231 records, respectively, were mediated by processes internal to the oceans rather than the continued,
232 elevated supply of nutrients from rivers. Such internal processes could be lower oxygen solubility,
233 changes in ocean circulation under a warming climate, and/or the enhanced recycling of bio-
234 essential nutrients, such as phosphorus, under more reducing conditions.

235 The Tl isotope trends during the negative CIE (i.e., the traditional T-OAE interval) also
236 suggest that global bottom water redox did not remain constant over the event. The shift from -3.5
237 to -2 and a return to -3.5, observed both in Canada and Germany, indicate another deoxygenation
238 event and decrease in the global burial of Mn-oxides (Fig. 3). This perturbation likely occurred
239 over approximately 30 to 50 kyr assuming the timescale of refs. 50 and 55 (the T-OAE negative
240 CIE has been assigned a duration of ~300 to 500 kyr, which locally is represented in ~4.5m in
241 Alberta) and linear sedimentation rates in Canada (from 11.345 to 11.84 m in the section) (49).
242 The continued positive shift in the Tl isotope data during the recovery limb of the negative CIE of
243 the T-OAE would require further marine deoxygenation and an additional ~25% reduction in
244 global Mn-oxide burial (34). The dissolution of Mn-oxides could be driven by permanent anoxia
245 or more realistically, transient deoxygenation that includes seasonal, centennial, and/or longer
246 timescales depending on local hydrography, water chemistry, and sedimentation rates. Both the
247 Pliensbachian/Toarcian Boundary and the onset of the traditional T-OAE interval are associated
248 with increased Mn/Ca values (56, 57), which could be due to the increased dissolved Mn reservoir
249 associated with the dissolution of Mn-oxides and reduction of Mn-oxide precipitation.

250 The traditional T-OAE interval (i.e., as defined by the negative CIE) is associated with the
251 main phase of Karoo-Ferrar LIP magmatism (50, 52, 58). This magmatic pulse would have caused
252 global warming and enhanced continental weathering, as suggested by numerical modeling and

253 geochemical and sedimentological records (49, 54, 59, 60). The net result would have been marine
254 eutrophication and intensified and more widespread oxygen minima (e.g., 5, 49, 60). The second
255 ε^{205}Tl shift during the rising limb of the T-OAE CIE is roughly coincident with previously
256 interpreted maximum extents of water-column sulfidic anoxia (i.e., euxinia) during this event (31,
257 61). This second deoxygenation event corresponds to a further decline in marine diversity (end of
258 phase 3 in ref. 19)—that is, a continuation and ultimately the acme of the event that started at the
259 Pliensbachian/Toarcian boundary (17, 18, 62–64) (Fig. 4). Given that these major losses in marine
260 diversity occur coincidently with changes observed in the Tl isotope record (Fig. 4), ocean
261 deoxygenation is implied as a significant or even the ultimate driver of extinction during this time.
262 This interpretation does not, however, preclude a role by other environmental changes that may
263 have occurred over this time in response to increasing pCO_2 (e.g., global warming and ocean
264 acidification).

265 Interestingly, the ε^{205}Tl data do not immediately return to pre-event values after the peak
266 of the positive CIE and remain high through the *Harpoceras falciferum* and lower *Hildoceras*
267 *bifrons* ammonite Zones as δ^{13}C declines (Fig. 3). A similar pattern has been observed in the Tl
268 isotope record of OAE-2 marked by values that remain high well after the end of the positive CIE
269 (38). The decoupling of the two isotope systems suggests that global Mn-oxide burial remained
270 low and bottom-water oxygen minima continued well after the termination of globally enhanced
271 organic carbon burial rates during both OAEs.

272 One interpretation for this observation could be that while overall organic carbon burial
273 declined, productivity was sufficiently high to maintain the consumption of deeper water oxygen
274 renewal (41). This scenario seems to be supported by the Os isotope record, which also remains
275 elevated above pre-event values over this same interval (49, 54) and indicates continued elevated

continental weathering rates. Thus, the continued enhanced delivery of nutrients from weathering on the continents would have fueled elevated primary production that could have maintained the widespread expanded marine anoxia. Alternatively, large amounts of near-surface organic matter previously deposited during the event could have continued to drive bottom-water oxygen consumption and Mn-oxide dissolution during a time when new organic matter burial waned. This mechanism may also explain the elevated rates of pyrite burial inferred from the carbonate-associated-sulfate sulfur isotope records that persist well after the CIE in both the T-OAE (61) and OAE-2 (65). Consumption of organic matter in shallowly buried sediments might have fueled marine anoxia and pyrite burial well after the CIEs, irrespective of the flux of newly exported organic matter.

Conclusions

The Tl isotope data presented here reveal a more nuanced and explicit evidence for marine deoxygenation in the interval that surrounds the T-OAE, which began at the Pliensbachian/Toarcian boundary and expanded oxygen minima were sustained throughout the early Toarcian and well after the traditionally defined T-OAE interval. Since the Tl isotope excursion begins at the Pliensbachian/Toarcian boundary and generally corresponds with 1) the initiation of massive volcanism, 2) a brief but significant increase in continental weathering, and 3) the start of the protracted early Toarcian mass extinction event (19). Thus, this evidence for global marine deoxygenation provides a mechanism for the observed extinction record. Further, the current definition of the beginning of T-OAE, based on the start of the negative CIE and/or first occurrence of black shales in Europe, represents the nadir of the deterioration of environmental conditions, but not the onset of global deoxygenation.

The concept of an OAE was proposed due to the realization that the preservation of organic matter in marine sediments might not always be the product of local conditions. It followed that carbon isotope excursions became the signature of enhanced burial of organic carbon on a global scale. Our study highlights the need to revisit our definition of the temporal OAE and consider whether for the record of oceanic anoxia might be better defined by other geochemical proxies that reconstruct specific redox states of the global ocean. Perhaps more importantly, the acknowledgment that global deoxygenation may expand beyond the traditionally defined OAEs has important implications for our understanding of the environmental feedbacks that lead to and maintain these events. Identifying such processes would be key to determining the consequences and potential endpoints of the recent trend in deoxygenation in the oceans today.

ACKNOWLEDGMENTS

TRT would like to thank the FSU Arts and Sciences Postdoctoral Fellowship, GSA, AAPG, SEPM, and Virginia Tech for funding. Grants to BCG (NSF EAR-1324752), JDO and SGN (NSF OCE-1624895 and NASA NNX16AJ60G), and TWL (NSF EAR-0719911) also funded this work. A portion of this work was performed at the National High Magnetic Field Laboratory, which is supported by National Science Foundation Cooperative Agreement No. DMR-1157490 and the State of Florida. We thank Hannah Grove, Brett Holdaway, and Ashley Prow for laboratory assistance. Alberta outcrop collections were authorized by the following permits: Parks Canada, Permit No: YHTR-2014-16156; RTMP, Permit No: 13-058, 14-009, 15-019. Finally, we would like to thank two anonymous reviewers whose comments greatly improved the manuscript.

Author Contributions

TRT, BCG, and JDO designed the study. TRT, AHC, AMG, BCG, and SMM collected samples. AHC identified the ammonites. TRT, BCG, SMM, and JDO conducted the geochemical analyses. TRT wrote the paper with significant contributions from all the authors.

References and Notes:

1. Schmidtko S, Stramma L, Visbeck M (2017) Decline in global oceanic oxygen content during the past five decades. *Nature* 542:335–339.
2. Breitburg D, et al. (2018) Declining oxygen in the global ocean and coastal waters. *Science* 359:eaam7240.
3. Pálfy J, Smith PL (2000) Synchrony between Early Jurassic extinction, oceanic anoxic event, and the Karoo-Ferrar flood basalt volcanism. *Geol* 28:747–750.
4. Takashima R, Nishi H, Huber, BT, Leckie RM (2006) Greenhouse world and the Mesozoic ocean. *Ocean* 19:64–74.
5. Jenkyns HC (2010) Geochemistry of oceanic anoxic events. *Geochem Geophys Geosys* 11:Q03004.
6. Rothman DH (2017) Thresholds of catastrophe in the Earth system. *Sci Adv* 3:e1700906.
7. Keeling RF, et al. (2010) Ocean deoxygenation in a warming world. *Ann Rev Mar Sci* 2:199–229.
8. Long MC, et al. (2016) Finding forced trends in oceanic oxygen. *Glob Biogeochem Cyc* 30:381–397.
9. Schlanger SO, Jenkyns HC (1976) Cretaceous Oceanic Anoxic Events: Causes and Consequences. *Geol Mijn* 55:179–184.

10. Scholle PA, Arthur MA (1980) Carbon Isotope Fluctuations in Cretaceous Pelagic Limestones: Potential Stratigraphic and Petroleum Exploration Tool. *Am Assoc Petr Geol Bull* 64:67–87.

11. Schlanger SO, Arthur MA, Jenkyns HC, Scholle PA (1987) The Cenomanian-Turonian Oceanic Anoxic Event, I. Stratigraphy and distribution of organic carbon-rich beds and the marine $\delta^{13}C$ excursion. *Mar Pet Sour Rocks*, eds Brooks J, Fleet AJ (Geological Society, London) Special Publications, Vol 26, pp 371–399.

12. Arthur MA, Dean WE, Pratt LM (1988) Geochemical and climatic effects of increased marine organic carbon burial at the Cenomanian/Turonian boundary. *Nature* 335:714–717.

15. Jenkyns HC (1988) The early Toarcian (Jurassic) Anoxic Event: Stratigraphic, sedimentary, and geochemical evidence. *Am J Sci* 19:101–151.

16. Hesselbo SP, et al. (2000) Massive dissociation of gas hydrate during a Jurassic oceanic anoxic event. *Nature* 406:392–395.

17. Harries PJ, Little CTS (1999) The early Toarcian (Early Jurassic) and the Cenomanian-Turonian (Late Cretaceous) mass extinctions: similarities and contrasts. *Palaeogeo Palaeoclim Palaeoecol* 154:39–66.

18. Dera G, et al. (2010) High-resolution dynamics of Early Jurassic marine extinctions: the case of Pliensbachian-Toarcian ammonites (Cephalopoda). *J Geol Soc Lon* 167:21–33.

19. Caruthers AH, Smith PL, Gröcke DR (2013) The Pliensbachian-Toarcian (Early Jurassic) extinction, a global multi-phased event. *Palaeogeo Palaeoclim Palaeoecol* 386:104–118.

20. Hermoso M, et al. (2009) Expression of the Early Toarcian negative carbon-isotope excursion in separated microfractions (Jurassic, Paris Basin). *Earth Plan Sci Lett* 277:194–203.

21. Them TR II, et al. (2017) High-resolution carbon isotope records of the Toarcian Oceanic Anoxic Event (Early Jurassic) from North America and implications for the global drivers of the Toarcian carbon cycle. *Earth Plan Sci Lett* 459:118–126.

22. Kump LR, Arthur MA (1999) Interpreting carbon-isotope excursions: carbonates and organic matter. *Chem Geol* 161:181–198.

23. Tyson RV (2005) The "Productivity versus Preservation" controversy: Causes, flaws, and resolution. *SEPM Spec Pub No 82*. The Deposition or Organic-Carbon-Rich Sediments: Models, Mechanisms, and Consequences. pp 17–33.

24. Middelburg JJ, Vlug T, Jaco F, van der Nat, WA (1993) Organic matter mineralization in marine sediments. *Glob Plan Ch* 1-2:47–58.

25. Burdige DJ (2007) Preservation of Organic Matter in Marine Sediments: Controls, Mechanisms, and an Imbalance in Sediment Organic Carbon Budgets? *Chem Rev* 109:467–485.

26. Canfield DE (1994) Factors influencing organic carbon preservation in marine sediments: *Chem Geol* 114:315–329.

27. Hartnett HE, Keil RG, Hedges JI, Devol AH (1998) Influence of oxygen exposure time on organic carbon preservation in continental margin sediments: *Nature* 391:572–574.

28. Schouten S, et al. (2000) Effects of an oceanic anoxic event on the stable carbon isotopic composition of early Toarcian carbon. *Am J Sci* 300:1–22.

29. Pearce CR, Cohen AS, Coe AL, Burton, KW (2008) Molybdenum isotope evidence for global ocean anoxia coupled with perturbations to the carbon cycle during the Early Jurassic. *Geol* 36:231–234.

30. French KL, Sepúlveda J, Trabucho-Alexandre J, Gröcke DR, Summons RE (2014) Organic geochemistry of the early Toarcian oceanic anoxic event in Hawsker Bottoms, Yorkshire, England. *Earth Plan Sci Lett* 390:116–127.

31. Dickson AJ, et al. (2017) Molybdenum isotope chemostratigraphy and paleoceanography of the Toarcian Oceanic Anoxic Event (Early Jurassic). *Paleocean* 32:813–829.

32. Rehkämper M, et al. (2002) Thallium isotope variations in seawater and hydrogenetic, diagenetic, and hydrothermal ferromanganese deposits. Earth *Plan Sci Lett* 197:65–81.

33. Nielsen SG, Rehkämper M, Norman MD, Halliday AN, Harrison D (2006) Thallium isotopic evidence for ferromanganese sediments in the mantle source of Hawaiian basalts. *Nature* 439:314–317.

34. Owens JD, Nielsen SG, Horner TJ, Ostrander CM, Peterson LC (2017) Thallium-isotopic compositions of euxinic sediments as a proxy for global manganese-oxide burial. *Geochim Cosmochim Acta* 213:291–307.

35. Nielsen SG, Rehkämper M, Prytulak J (2017) Investigation and application of thallium isotope fractionation. *Rev Min Geochem* 82:759–798.

36. Nielsen SG, et al. (2011) Thallium isotopes in early diagenetic pyrite – A paleoredox proxy? *Geochim Cosmochim Acta* 75:6690–6704.

37. Nielsen SG, et al. (2013) Towards an understanding of thallium isotope fractionation during adsorption to manganese oxides. *Geochim Cosmochim Acta* 117:252–265.

38. Peacock CL, Moon EM (2012) Oxidative scavenging of thallium by birnessite: Explanation for thallium enrichment and stable isotope fractionation in marine ferromanganese precipitates. *Geochim Cosmochim Acta* 84:297–313.

39. Rehkämper M, Frank M, Halliday A. (2004) Cenozoic marine geochemistry of thallium

deduced from isotopic studies of ferromanganese crusts and pelagic sediments. *Earth Plan Sci Lett* 219:77–91.

40. Nielsen, SG et al. (2006) Hydrothermal fluid fluxes calculated from the isotopic mass balance of thallium in the ocean crust. *Earth Plan Sci Lett* 1-2:120–133.

41. Ostrander CM, Owens JD, Nielsen SG (2017) Constraining the rate of oceanic deoxygenation leading up to a Cretaceous Oceanic Anoxic Event (OAE-2: ~94Ma). *Sci Adv* 3:e1701020.

42. Nielsen SG, et al. (2009) Thallium isotope evidence for a permanent increase in marine organic carbon export in the early Eocene. *Earth Plan Sci Lett* 278:297–307.

43. Rue EL, Smith GJ, Cutter GA, Bruland KW (1997) The response of trace element redox couples to suboxic conditions in the water column. *Deep Sea Res Part I: Ocean Res Pap* 44:113–134.

45. McArthur JM, Algeo TJ, vd Schootbrugge B, Li Q, Howarth RJ (2008) Basinal restriction, black shales, Re-Os dating, and the Early Toarcian (Jurassic) oceanic anoxic event. *Paleocean* 23:PA4217.

46. Bura-Nakić E, et al. (2018) Coupled U-Mo abundances and isotopes in a small marine euxinic basin: Constraints on processes in euxinic basins. *Geochim Cosmochim Acta* 222:212–229.

47. Owens JD, Reinhard CT, Rohrssen M, Love GD, Lyons, TW (2016) Empirical links between trace metal cycling and marine microbial ecology during a large perturbation to Earth's carbon cycle. *Earth Plan Sci Lett* 449:407–417.

48. Röhl H-J, Schmid-Röhl A, Oschmann W, Frimmel A, Schwark L (2001) The Posidonia Shale (Lower Toarcian) of SW-Germany: an oxygen-depleted ecosystem controlled by sea

level and palaeoclimate. *Palaeogeo Palaeoclim Palaeoecol* 169:273–299.

49. Them TR, et al. (2017) Evidence for rapid weathering response to climatic warming during the Toarcian Oceanic Anoxic Event. *Sci Rep* 7:5003.

50. Sell B, et al. (2014) Evaluating the temporal link between Karoo LIP and climatic-biologic events of the Toarcian Stage with high-precision U-Pb geochronology. *Earth Plan Sci Lett* 408:48–56.

51. Ruhl M, et al. (2016) Astronomical constraints on the duration of the Early Jurassic Pliensbachian Stage and global climatic fluctuations. *Earth Plan Sci Lett* 455:149–165.

52. Moulin M, et al. (2017) Eruptive history of the Karoo lava flows and their impact on early Jurassic environmental change. *J Geophys Res Sol Earth* 2011JB008210.

53. Xu W, et al. (2018) Magnetostratigraphy of the Toarcian Stage (Lower Jurassic) or the Llandbedr (Mochras Farm) Borehole, Wales: basis for a global standard and implications for volcanic forcing of palaeoenvironmental change. *J Geol Soc* jgs:2017-120.

54. Percival LME, et al. (2016) Osmium isotope evidence for two pulses of increased continental weathering linked to Early Jurassic volcanism and climate change. *Geol* 44:759–762.

55. Boulila S, et al. (2014) Astronomical calibration of the Toarcian Stage: Implications for sequence stratigraphy and duration of the early Toarcian OAE. *Earth Plan Sci Lett* 386:98–111.

56. Hermoso M. et al. (2009) Global and local forcing of Early Toarcian seawater chemistry: A comparative study of different paleoceanographic settings (Paris and Lusitanian basins). *Paleocean* 24:PA4208.

57. Lu, Z, Jenkyns HC, Rickaby REM (2010) Iodine to calcium ratios in marine carbonate as a paleo-redox proxy during oceanic anoxic events. *Geol* 38:1107–1110.

58. Burgess SD, Bowring SA, Fleming TH, Elliot DH (2015) High-precision geochronology links the Ferrar large igneous province with early-Jurassic ocean anoxia and biotic crisis. *Earth Plan Sci Lett* 415:90–99.

59. Dera G, Donnadieu Y (2012) Modeling evidence for global warming, Arctic seawater freshening, and sluggish oceanic circulation during the Early Toarcian anoxic event. *Paleocean* 27:PA2211.

60. Izumi K, Kemp DB, Itamiya S, Inui M (2018) Sedimentary evidence for enhanced hydrological cycling in response to rapid carbon release during the early Toarcian oceanic anoxic event. *Earth Plan Sci Lett* 481:162–170.

61. Gill BC, Lyons TW, Jenkyns HC (2011) A global perturbation to the sulfur cycle during the Toarcian Oceanic Anoxic Event. *Earth Plan Sci Lett* 312:484–496.

62. Little CTS, Benton MJ (1995) Early Jurassic mass extinction: A global long-term event. *Geol.* 23:495–498.

63. Aberhan M, Baumiller TK (2003) Selective extinction among Early Jurassic bivalves: A consequence of anoxia. *Geol* 31:1077–1080.

64. Caswell BA, Coe AL, Cohen AS (2009) New range data for marine invertebrate species across the early Toarcian (Early Jurassic) mass extinction. *J. Geol. Soc.* 166:859–872.

65. Owens JD, et al. (2013) Sulfur isotopes track the global extent and dynamics of euxinia during Cretaceous Oceanic Anoxic Event 2. *Proc Nat Acad Sci* 110:18407–18412.

66. Scotese CR (2001) Atlas of Earth History PALEOMAP Project, Arlington, TX.

67. Dera G, et al. (2009) Water mass exchange and variations in seawater temperature in the NW Tethys during the Early Jurassic: Evidence from neodymium and oxygen isotopes of fish teeth and belemnites. *Earth Plan Sci Lett* 286:198–207.

Fig. 1: A) Idealized Pliensbachian and Toarcian carbon isotope stratigraphy (derived from multiple $\delta^{13}C$ records from Europe and North America shown in SI Fig. 3). Note the long-term positive CIE predating the negative CIE associated with the classic T-OAE interval.

Fig. 2: Global paleogeography of early Toarcian (modified from refs. 21, 49, 66). Black circles represent the study areas. Dashed extent of the Karoo-Ferrar LIP shown in southern Pangaea. Dark grey represents landmasses, light blue: shallow seas, and dark blue: open oceans. CPM = Central Pangaean Mountains.

Fig. 3: Chemostratigraphy of the Lower Jurassic Fernie Formation from East Tributary of Bighorn Creek Alberta and of the Lower Jurassic Posidonia Shale from the Dotternhausen Quarry in Germany. $\delta^{13}C_{org}$ = organic carbon isotopic compositions from refs. 21 and 31. Fe_{HR}/Fe_T = amount of highly reactive iron relative to total iron, and Fe_{Py}/Fe_{HR} = amount of pyrite iron relative to highly reactive iron (see SI Materials and Methods for discussion of this redox proxy). $\varepsilon^{205}Tl$ = thallium isotopic composition of seawater during deposition. Lithostratigraphic members of the Fernie Formation, Stages of the Jurassic, and ammonite zonations for both northwestern Europe and western North American shown to the left of the stratigraphic column (refer to ref. Them17a and SI Text for the details of their placements). Vertical gray line in ^{205}Tl records are the modern $^{205}Tl_{SW}$ composition of ~ -6 (34). Light gray $\varepsilon^{205}Tl$ values in the German section are from lithologies that are not ideal for metal isotope studies (low TOC < 0.3%.), and we therefore do not interpret these as primary oceanographic signals (see SI Text). Gray boxes represent CIE intervals.

505

506 **Fig. 4:** Sequence of events culminating in the Early Jurassic T-OAE (as delineated by changes in
507 the precipitation of manganese oxyhydroxides at the sediment-water interface, documented by
508 shifts in the $\varepsilon^{205}Tl$ composition of anoxic sediments) and carbon burial event (as delineated by
509 changes to the global carbon cycle, documented by changes in the $\delta^{13}C$ of organic and inorganic
510 carbon). As the Karoo-Ferrar LIP is emplaced (3, 52, 57), global ocean deoxygenation may occur
511 concurrently as sea surface temperatures rise (67). Massive injections of greenhouse gases and
512 cascading biogeochemical feedbacks cause the second decline in biodiversity associated with the
513 T-OAE negative CIE interval. The extent of anoxic marine bottom waters increases as
514 bioproductivity increases due to increased continental weathering and delivery of nutrients to the
515 oceans (49, 54), leading to the increased geographic extent of euxinia (31, 61), culminating in an
516 interval of maximum organic carbon burial, which causes the positive CIE. Increased oceanic
517 anoxia occurs concurrently with the onset of the main extinction event at the
518 Pliensbachian/Toarcian boundary (19, 63), and the greatest extent of anoxia and euxinia occurs
519 during the large, negative CIE interval (61, *this study*). White arrows represent "Phase 2" of the
520 Karoo-Ferrar eruptive scenario (52). Timescale is derived from ref. 51.

521

522

523 **Supplementary Materials:** Methods and Materials, Supplementary Text, Figures S1, S2, S3,
524 References, Databases S1 to S4.

525

526 **Additional Information**

527 **Competing financial interests:** The authors declare no competing financial interests

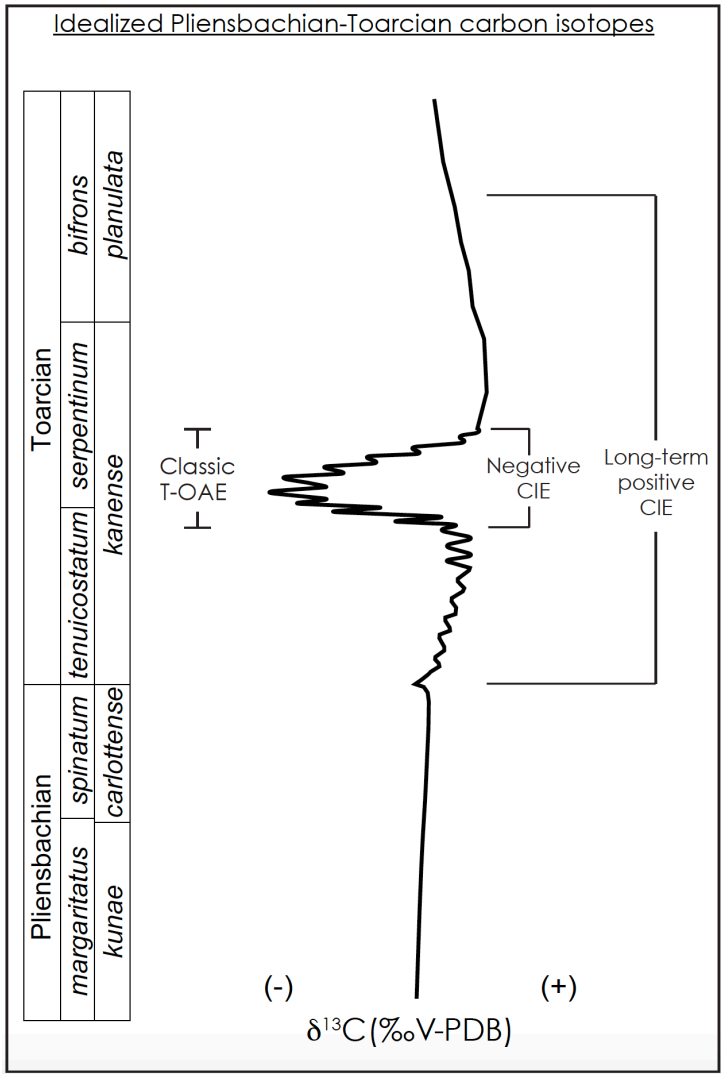
Idealized Pliensbachian-Toarcian carbon isotopes
Toarcian
Pliensbachian
bifrons
planulata
serpentinum
tenuicostatum
kanense
spinatum
carlottense
margaritatus
kunae
Classic
T-OAE
Negative
CIE
Long-term
positive
CIE
(-)
(+)
δ13C (‰V-PDB)

Fig. 1

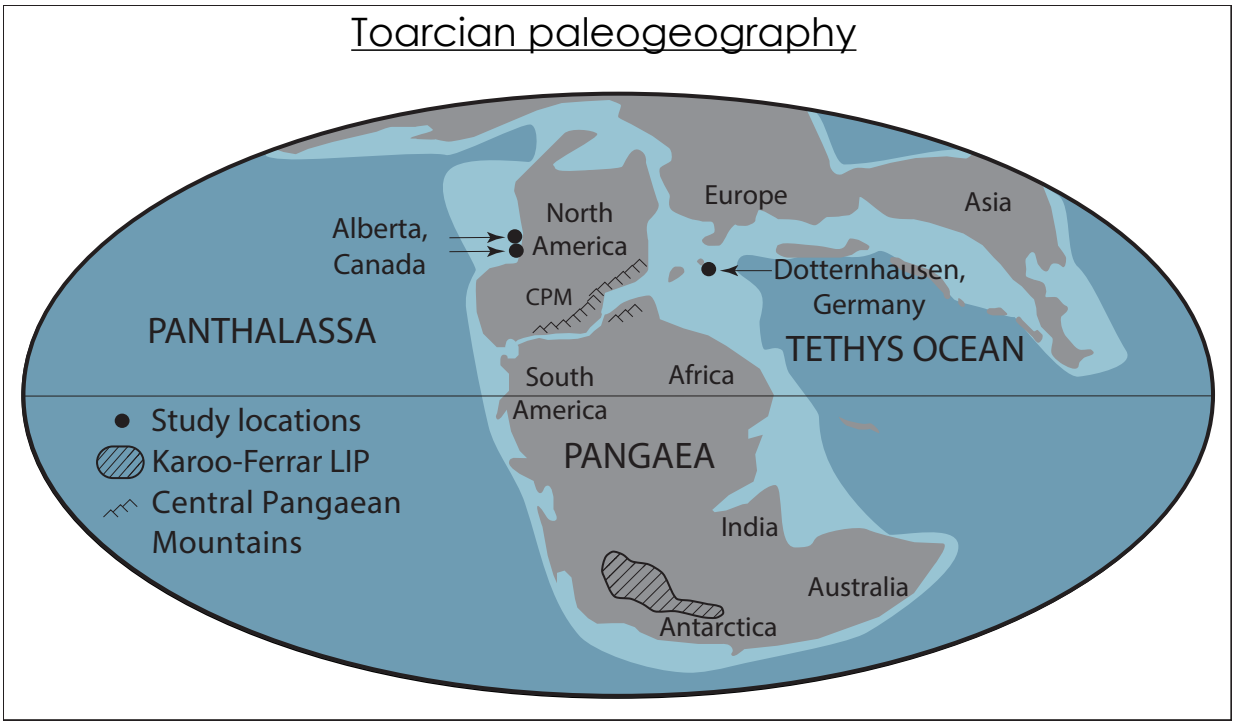
Toarcian paleogeography
Alberta,
Canada
North
America
Europe
Asia
Dotternhausen,
Germany
CPM
PANTHALASSA
TETHYS OCEAN
South
America
Africa
Study locations
Karoo-Ferrar LIP
Central Pangaean
Mountains
PANGAEA
India
Australia
Antarctica

Fig. 2

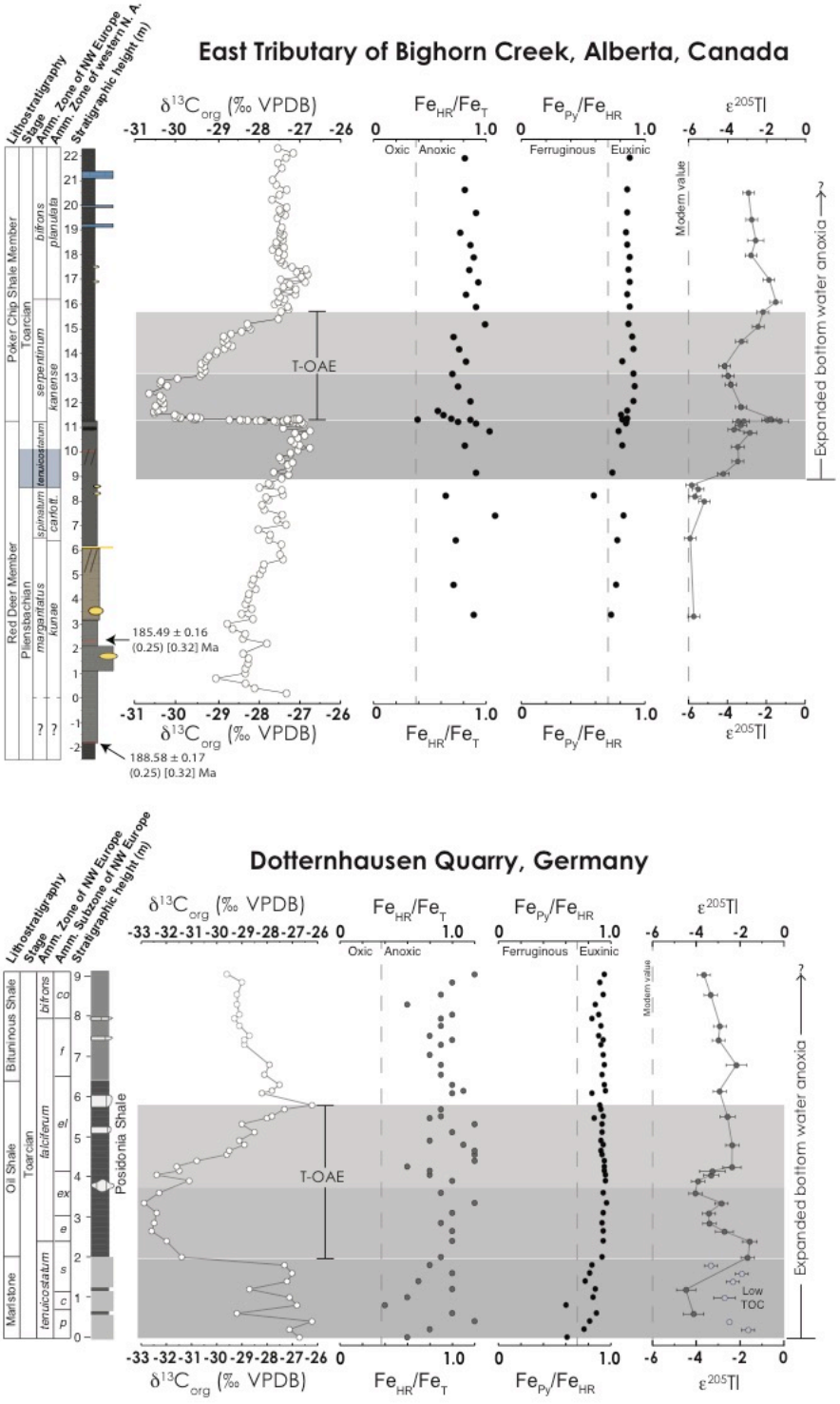

551

552 Fig. 3

553

554

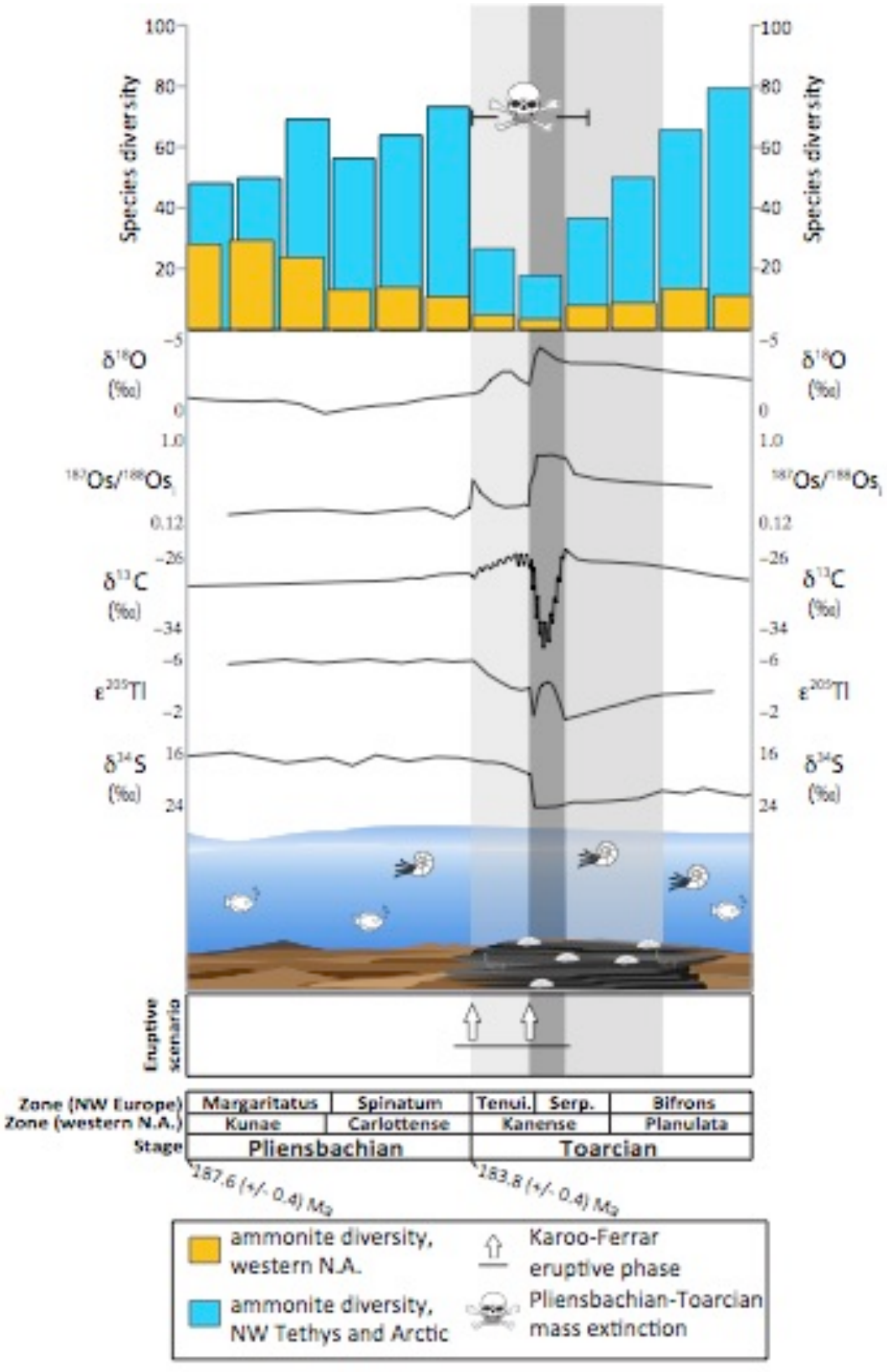
Species diversity
100
80
60
40
20
δ18O (‰)
−5
0
1.0
187Os/188Osi
0.12
δ13C (‰)
−26
−34
ε205Tl
−6
−2
δ34S (‰)
16
24
Eruptive scenario
Zone (NW Europe)
Zone (western N.A.)
Stage
Margaritatus
Spinatum
Tenui.
Serp.
Bifrons
Kunae
Carlottense
Kanense
Planulata
Pliensbachian
Toarcian
187.6 (+/- 0.4) Ma
183.8 (+/- 0.4) Ma
ammonite diversity, western N.A.
ammonite diversity, NW Tethys and Arctic
Karoo-Ferrar eruptive phase
Pliensbachian-Toarcian mass extinction

555

556 Fig. 4

Supplementary Materials for

Thallium isotopes reveal protracted anoxia associated with volcanism, carbon burial and extinction during the Toarcian (Early Jurassic)

Theodore R. Them II, Benjamin C. Gill, Andrew H. Caruthers, Angela M. Gerhardt, Darren R. Gröcke, Timothy W. Lyons, Selva M. Marroquín, Sune G. Nielsen, João P. Trabucho Alexandre, and Jeremy D. Owens

correspondence to: tthem@fsu.edu

This PDF file includes:

Other Supplementary Materials for this manuscript includes the following:

Database S1: Geochemistry for East Tributary section.
Database S2: Geochemistry for drill core 1-35-62-20W5.
Database S3: Geochemistry for drill core 6-32-75-5W6.
Database S4: Geochemistry for Dotternhausen section.

Materials and Methods

Sampling Locations and Materials

Published accounts of the collective lithostratigraphy, ammonite biostratigraphy, U-Pb zircon age dates, and high-resolution carbon isotope chemostratigraphy for the East Tributary and Dotternhausen Quarry can be found in refs. 1, 2, 3, 4. Here, we discuss and summarize key aspects of these analyses as they pertain to our study.

Drill cores 1-35-62-20W5 and 6-32-78-5W6 (SI Figs. 1, 2) of the Fernie Formation were described and sampled for geochemical analyses at the Core Research Centre in Calgary, Alberta, Canada. They contain the Pliensbachian to lower Toarcian Gordondale and Poker Chip Shale (PCS) members, and have been correlated by geophysical gamma ray logs, ammonites, and carbon isotopes to outcrops of Red Deer and PCS, including East Tributary (1, 5, 6). Each core contains mixed organic-rich calcareous mudstones and siltstones in the Gordondale Member, which are overlain by organic-rich calcareous mudstones of the PCS (5).

Core 1-35-62-20W5 contains alternating organic-rich calcareous siltstones and mudstones (SI Fig. 1) of the Gordondale and PCS members. The Gordondale Member ranges from the base of the core to 2029 m and contains several bivalve beds (5) and the Pliensbachian (Freboldi Zone) ammonite *Dubariceras* cf. *silviesi* at 2033.3 m. The PCS Member comprises 2029 m to the top of the core (5) and contains organic-rich calcareous mudstones, displacive and diagenetic carbonate cements and fans, with abundant bivalves, the cephalopod *Actractites*, and the Toarcian ammonite Dactylioceras sp. at 2027.1 m (5).

Core 6-32-78-5W6 contains alternating organic-rich calcareous siltstones and mudstones (SI Fig. 2) of the Gordondale and PCS members. The Gordondale Member ranges from the base of the core to ~1219 meters (5) and contains several bivalve beds[5], the Pliensbachian ammonite *Amaltheus* sp. at 1221.8 m, and Toarcian Kanense to Planulata Zone equivalent *Dactylioceras cf. crosbeyi* and *Cleviceras exaratum* at 1217.9 and 1217.8 meters, respectively. From 1221 to 1219 m, the dominant lithology is an organic-rich mudstone, with a thin, organic-rich, silty mudstone capped by a displacive carbonate fan around 1220.25 m. From 1219 to 1214.6 m, the dominant lithology is an organic-rich, laminated, calcareous siltstone, with many bitumen-rich intervals. The PCS Member comprises 1214.6 m to the top of the core (5) and contains organic-rich calcareous mudstones, rare bivalves, and often contains intervals that are laminated.

These sections represent an excellent opportunity to use the Toarcian CIE as an intra-basinal and a global chemostratigraphic marker (SI Fig. 3); since these cores represent time-correlative, deeper-water facies to the East Tributary section (5), it is possible to reconstruct paleoceanographic dynamics across the T-OAE. Specifically, if redox variations change with paleo-water depth, and potentially temporally, then it should be possible to reconstruct the temporal and spatial extent of oxygenation within the basin.

Total organic carbon contents (TOC) and isotope compositions ($\delta^{13}C_{org}$)

Carbon-isotope and total organic carbon content data of the East Tributary and Dotternhausen sites were recently reported by refs. 1, 2 and ref. 4, respectively. The new data presented here are from the 1-35-62-20W5 and 6-32-78-5W6 drill cores and follow the methods in refs. 1, 2, 4.

Powders were obtained from the drill core and outcrops samples either using a handheld Dremel tool with a diamond tip drill bit or a ball mill using a silica nitride ceramic vial set. To remove the carbonate fraction, several milliliters of 2N HCl were added to ~0.1 g of powder and allowed to react for ~24 hours. The solution was rinsed until a neutral pH was obtained, and then

the samples were dried in an oven.

$\delta^{13}C_{org}$ and total organic carbon (TOC) values of the carbonate-free sample residues were conducted on an Isotope Cube elemental analyzer connected to an Isoprime 100 gas source isotope-ratio mass spectrometer (IRMS) in the Sedimentary Geochemistry Isotope Laboratory in the Department of Geosciences at Virginia Tech. The isotope compositions of the samples were expressed in the standard delta (δ) notation as per mil deviations (‰) from Vienna Pee Dee Belemnite (VPDB) and calculated such that:

$$\delta^{13}C=[((^{13}C/^{12}C)_{sample} - (^{13}C/^{12}C)_{standard}) / (^{13}C/^{12}C)_{standard}] \times 1000 \qquad \textbf{Eq. 1}$$

Samples were calibrated to the VPDB scale using international (IAEA-CH-6 and IAEA-CH-7) and commercial standards (Elemental Microanalysis wheat flour, sorghum flour, low organic soil, and urea). Long-term analytical precision for the $\delta^{13}C$ measurements is <0.1‰ based on replicated analyses on isotope standards: this provided a linear range in $\delta^{13}C$ between -48.66‰ and -10.42‰. Total organic carbon was obtained as part of the isotopic analysis using elemental standards (i.e., Acetanilide, 71.09% C). Approximately 66% of total samples (n = 86) from core 6-32-78-5W6 were replicated at least once. Approximately 91% of total samples (n = 78) from core 1-35-62-20W5 were replicated at least once. Average analytical uncertainty for replicated analyses (n = 128) was 0.07‰.

Iron speciation analysis

The amount of iron found in various mineral phases (iron speciation) of fine-grained siliciclastic units can be used to identify local modern and ancient water column redox conditions (7-10). Specifically, the amount highly reactive iron-bearing phases (Fe_{HR}; see Equation 2) can be quantified to determine local redox conditions during deposition (11). The Fe_{HR} pool represents available iron that reacts with aqueous sulfide to form pyrite (12). The highly reactive iron pool (e.g., 10) is defined as:

$$Fe_{HR} = Fe_{py} + Fe_{carb} + Fe_{ox} + Fe_{mag} \qquad \textbf{Eq. 2}$$

where Fe_{py} represents iron bound as pyrite; Fe_{carb} represents iron hosted in carbonate phases including calcite, siderite, and ankerite; Fe_{ox} represents iron hosted in the ferrihydrite, lepidocrocite, goethite, and hematite fractions; and Fe_{mag} represents iron hosted in the magnetite fraction.

Modern and ancient marine siliciclastic sediments deposited under an anoxic water column have a Fe_{HR}/Fe_T (Fe_T represents total iron in the sample) value of >0.38, whereas sediments deposited under an oxic water column are generally below 0.22 (7, 11, 13). Because the amount of pyrite that can be deposited in anoxic environments during the microbial reduction of sulfate (e.g., 12) can vary, the amount of Fe_{py} to Fe_{HR} in each sample can help discern whether the water column was ferruginous (pyrite formation limited by available sulfides) or euxinic (pyrite formation limited by available reactive iron). Fe_{py}/Fe_{HR} values > ~0.7-0.8 are indicative of water column euxinia, whereas Fe_{py}/Fe_{HR} values < ~0.7-0.8 are indicative of ferruginous conditions (11, 14, 15).

To determine the relative amount of iron in each iron-bearing phase, the sequential extraction method of ref. 8 was performed at the Department of Geosciences at Virginia Tech. For this procedure, approximately 0.1 grams of powder was used. First, Fe_{carb} was liberated by the

addition of a 10mL solution of 1M sodium acetate and acetic acid, buffered to pH of 4. These samples were placed on a shaking table for 48 hours at 50° C and then centrifuged. Next, Fe_{ox} was liberated from the samples by the addition of a 10mL solution of sodium dithionite and sodium citrate, buffered to pH of 4. These samples were placed on a shaking table for two hours, and then centrifuged. Finally, Fe_{mag} was liberated by the addition of a 10mL solution of ammonium oxalate. These samples were placed on a shaking table for six hours, and then centrifuged. After each extraction, 100 μL of the supernatant was transferred to a new tube, followed by the addition of 4 mL of HEPES, ferrozine, and hydroxylamine HCl solution (e.g., 16) and allowed to react overnight. All of the supernatant was removed in the original sample tubes before the next iron extraction. Iron concentrations were measured in a spectrophotometer and calculated by a matrix-matched standard curve (e.g., 17).

Fe_{py} values were determined by chromium reduction methods of ref. 18. For this procedure, approximately 0.1 grams of powder was added to a three-neck flask for a distillation extraction. Following the purging of headspace with nitrogen gas a solution of 40 mL of 1M chromous chloride and 20 mL of 6N HCl was added to the flask, and then allowed to react for two hours while heating under the nitrogen atmosphere. Any volatized sulfide quantitatively reacted with a zinc acetate solution to form zinc sulfide. Later, silver nitrate was added to this solution, which converted the zinc sulfide to silver sulfide. The amount of sulfide in the sample was then determined by gravimetry after filtration and drying of the silver sulfide. The amount of pyrite iron hosted in the original sample was then stoichiometrically calculated from the amount of extracted sulfide.

For the determination of Fe_T approximately 0.2 grams of powder was ashed at 900° C for 6-8 hours to remove any organic matter and other volatile phases. Approximately 0.1 grams of powder was partially dissolved using 4 mL of 12M HCl, and then placed in a trace metal clean Teflon Savillex digestion vessel on a hot plate and boiled for 36-48 hours (19). The sample and solution were added to centrifuge tubes and centrifuged. After centrifugation, 100 μL of the supernatant was transferred to a new tube and the same technique was used to measure iron concentrations using a spectrophotometer as stated previously.

Iron concentrations were calculated by a matrix-matched standard curve. New standard solutions were prepared for each analysis with iron standard concentrations at 0, 5, 10, 20, 30, 40 75, 150, and 300 ppm. The r^2 value of the standard curve was always above 0.999 and many instances was 1. Multiple analyses of the same solution yielded no error via spectrophotometer output, and no samples yielded higher iron concentrations than the standards. Sample reproducibility using this method is often ± 7% when analyzing different aliquots of the same extracted iron pool (e.g., 17).

Thallium isotope analysis

The precipitation of manganese oxides is directly controlled by available oxygen, and therefore ceases in low oxygen environments. As manganese oxide precipitation decreases during the onset of widespread deoxygenation in the oceans, changes the Tl elemental and isotopic budget are the first systems to be perturbed (20). To assess the global dynamics of oceanic oxygenation during the Early Jurassic, this study utilizes a novel isotopic system that is not fractionated by biological processes in the open ocean (*23*). Thallium has two naturally occurring isotopes: ^{203}Tl and ^{205}Tl. The thallium isotopic composition of a sample is compared to the NIST SRM 997 Tl standard and reported such that:

$$\varepsilon^{205}Tl = 10{,}000 \times (^{205}Tl/^{203}Tl_{sample} - ^{205}Tl/^{203}Tl_{SRM\ 997}) / (^{205}Tl/^{203}Tl_{SRM\ 997}) \qquad \textbf{Eq. 3}$$

To track manganese oxide burial during the Early Jurassic, chemical analysis (21, 22) was utilized to isolate thallium in a state-of-the-art clean laboratory at the National High Magnetic Field Laboratory at Florida State University. For this procedure, approximately 0.05 grams of sample powder (0.1 grams of standard SCO-1) was placed into a trace metal clean teflon savillex beaker with 3mL of 2M HNO_3 was added and placed on a hot plate for approximately 12 hours at 130° C. These samples were then centrifuged, and the supernatant was collected and placed in a new, clean savillex beaker, and dried. Care was taken to not collect siliciclastic materials, and to ensure limited siliciclastic Tl contamination HF was avoided. Several high-purity acid treatments (aqua regia, 50% conc. HCl or HNO_3 + H_2O_2) were added to each beaker to fully oxidize any organic matter present. These solutions were placed on hot plates at 120-130° C for several days if necessary. To completely oxidize samples for column chemistry, 1 M HCl and ~100 μL brominated H_2O were added to each beaker the previous night. All acids and reagents were trace metal grade to ensure low blank levels.

For column chemistry, we followed the method of refs. 23-25 (described below), but this dataset only used one micro-column procedure, which was shown to work well for high Tl and low Pb samples (22). For Pb removal, AG1X8 200-400 mesh resin was added to each column. This was followed by the addition of solutions 0.1 ml and 1.5 ml of each HCl-SO_2, 0.1M HCl, and 0.1 M HCl with 1% Br_2-H_2O. Samples were loaded into the columns, followed by the addition of 0.1 ml and 1.5 ml solutions of 0.5 M HNO_3 – 3% Br_2-H_2O, 2.0 M HNO_3 – 3% Br_2-H_2O, and 0.1 M HCl – 1% Br_2-H_2O. Thallium was then collected using 0.1 ml and 1.5 ml of 0.1 M HCl-SO_2 solution. Importantly, H_2SO_4 was evaporated at high temperature, and each sample was dissolved in a 0.1 M HNO_3 + 0.1% H_2SO_4 solution. A 10-μL aliquot of this solution was analyzed with an Agilent 7500cs ICP-MS to measure Pb and Tl abundances. Using these concentration data, sample concentrations were matched to within 25% of standard and spiked with an abundance of NIST SRM 997 Pb standard. Thallium isotope measurements were performed on a Thermo Neptune MC-ICP-MS at FSU. Approximately 90% of the samples were analyzed at least twice (some samples were not replicated due to sample limitation). The average 2σ standard deviation for all replicated samples is ± 0.25 epsilon units or better. The long-term average ε^{205}Tl value for the SCo-1 standard is -3.0 ± 0.3 and all of our SCo-1 values were within this range. Samples that had reproducibility under 0.3 were displayed with an uncertainty of 0.3 (long-term reproducibility of SCo-1 standard), and samples that had reproducibility above 0.3 are displayed with that specific uncertainty.

Supplementary Text

Revised placement of Pliensbachian-Toarcian boundary at East Tributary section

The original placement of the Pliensbachian-Toarcian boundary at East Tributary was placed at ~10.15 m based on the first appearance of the Toarcian ammonites *Cleviceras exaratum* and *Hildaites cf. murleyi* (1). However, the boundary could feasibly occur between ~8.5 m and 10.15 m, as this interval also includes ammonites that are known to span the Pliensbachian-Toarcian boundary in western North America (i.e., *Tiltoniceras cf. antiquum* and *Protogrammoceras paltum* (27, 28). Regardless of boundary placement our interpretations remain consistent in that water column deoxygenation predated the large negative CIE of the T-OAE, rather occurring at the Pliensbachian-Toarcian boundary over a time-frame that is coeval with phase 3 of the multi-phased Pliensbachian-Toarcian mass extinction (29) and supported by osmium isotope geochemical records (2, 30) and the absolute ages of the Pliensbachian-Toarcian boundary (2, 31, 32). Therefore, deoxygenation would still be considered as a major driver for the

main phase of this mass extinction event.

Positive carbon isotope excursion during the early Toarcian (pre-T-OAE CIE)

In Fig. 1 of the main text, the long-term, globally observed positive carbon isotope excursion during the early Toarcian is noted. This phenomenon is observed in inorganic and organic matter of marine and terrestrial carbon in several locations from Europe, Africa, and North America (1, 33-39) (Fig. S3). The new thallium isotope dataset from western Canada suggest that increased anoxia and burial of organic carbon were the mechanisms behind the long-term positive CIE beginning in the basal Toarcian.

Ammonite zones of new oceanic deoxygenation records

New Tl data from two geographically far removed anoxic basins suggest that the expansion of early Toarcian anoxic bottom began at the base of the correlative Tenuicostatum (northwest Europe and South America), Polymorphum (Mediterranean), Antiquum (High-Arctic), and Kanense (western North America) zones, and continued into the middle Toarcian at a correlative level with the Bifrons Zone of northwest Europe (see ref. 29).

Dotternhausen Quarry Tl isotopes

In Fig. 2 of the main text, several Tl isotope data points below the T-OAE CIE were displayed as light gray. These samples came from carbonate marls with extremely low TOC contents (0.34 – 0.78%) (4). Therefore, we compared only the two Tl isotope data points from the organic-rich black shales (pre-T-OAE) with the organic-rich black shales from the OAE and post-OAE interval. Interpreting the Tl-isotopic composition of the low TOC marls as a proxy for relative global manganese oxide burial is unexplored and could lead to erroneous conclusions as the Tl-isotope proxy (and other metal isotope proxies) have not been developed or tested in such depositional environments.

Yorkshire, UK Tl isotopes

The Tl-isotope results from our two new study sites cannot be directly compared with that of Yorkshire, UK (42). This is because of the interpreted severe basinal restriction that accompanied the T-OAE interval in the Cleveland Basin (43). The basinal restriction associated with this interval is demonstrated to have overprinted rhenium, osmium, and molybdenum systems, which has resulted in isotope stratigraphies that were not indicative of the global record (2, 4, 30, 43). Furthermore, the larger variations in the Tl-isotopes at Yorkshire (42) compared to western North America and Germany (this study) suggest the record is related to regional or local Mn-oxide burial events not well connected with the open ocean.

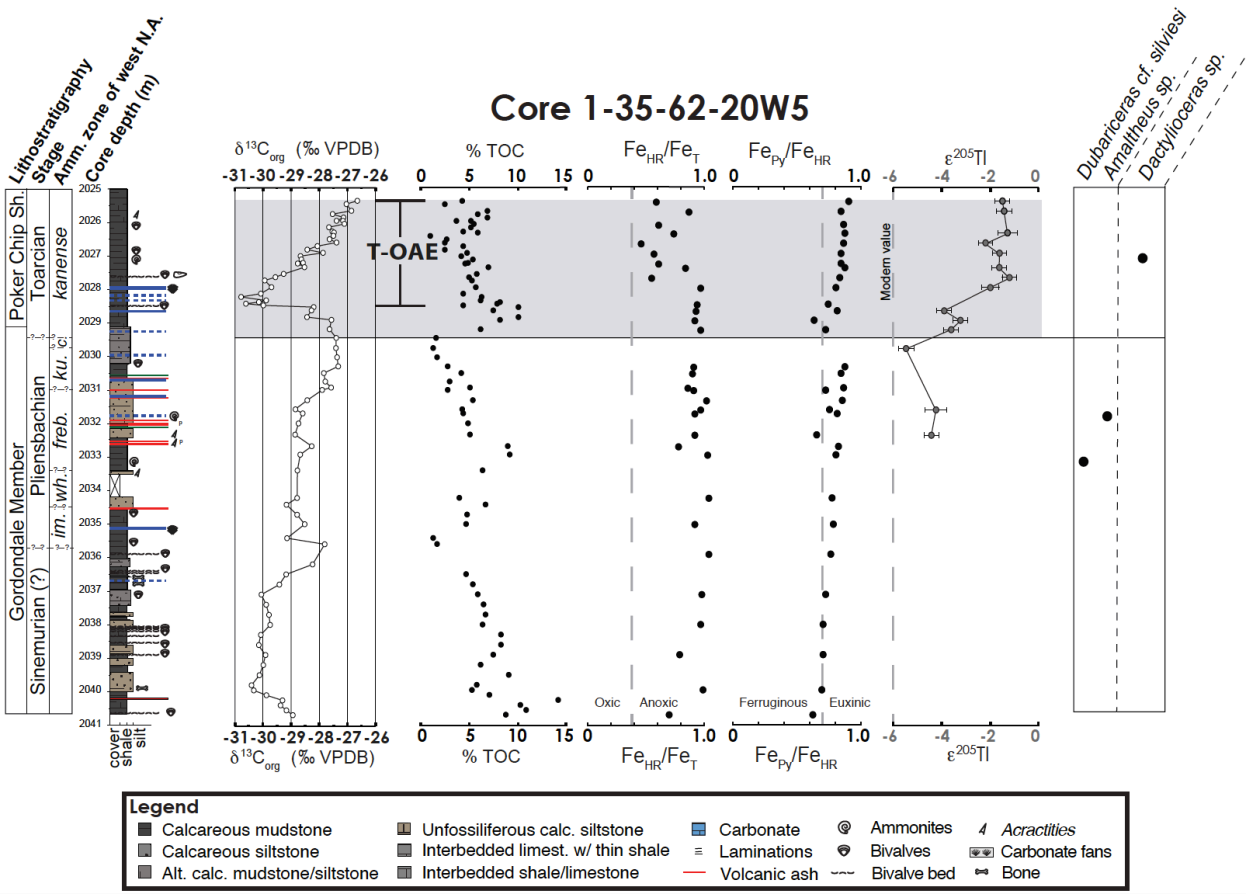

Fig. S1.

Litho- and Chemo-stratigraphies of the Lower Jurassic Fernie Formation from drill core 1-35-62-20W5, Alberta, Canada. $\delta^{13}C_{org}$ = organic carbon isotopic compositions. Fe_{HR}/Fe_T = amount of highly reactive iron relative to total iron, and Fe_{Py}/Fe_{HR} = amount of pyrite iron relative to highly reactive iron (see SI Materials and Methods for discussion of this local redox proxy). $\varepsilon^{205}Tl_{SW}$ = thallium isotopic composition of seawater during deposition. Lithostratigraphic members of the Fernie Formation, Stages of the Jurassic, and ammonite zonations for both northwestern Europe and western North American shown to the left of the stratigraphic column. Gray bar represents approximate expansion of deoxygenated bottom waters near the Pl-To boundary.

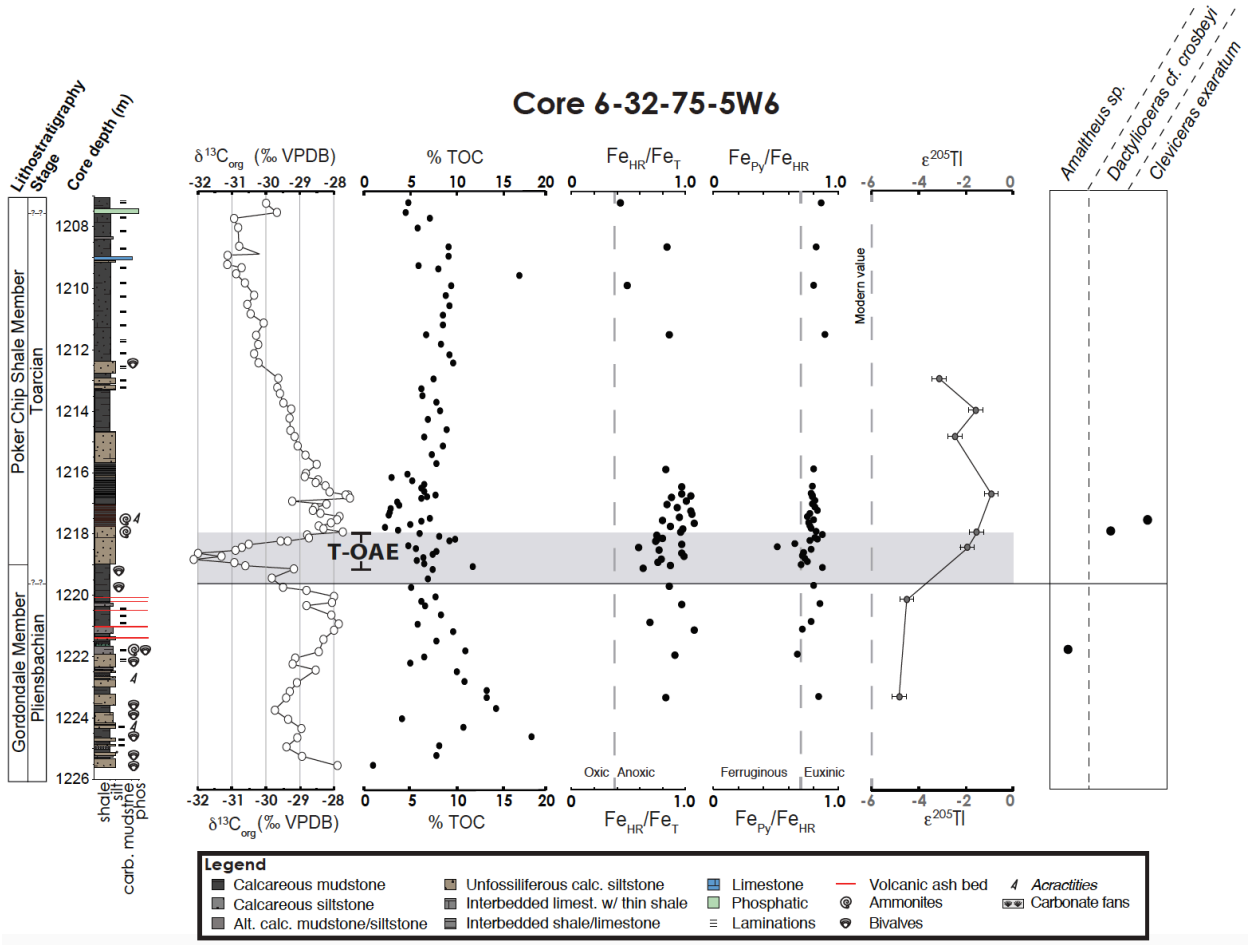

Fig. S2.

Litho- and Chemo-stratigraphies of the Lower Jurassic Fernie Formation from drill core 6-32-78-5W6, Alberta, Canada. $\delta^{13}C_{org}$ = organic carbon isotopic compositions. Fe_{HR}/Fe_T = amount of highly reactive iron relative to total iron, and Fe_{Py}/Fe_{HR} = amount of pyrite iron relative to highly reactive iron. $\varepsilon^{205}Tl_{SW}$ = thallium isotopic composition of seawater during deposition. Lithostratigraphic members of the Fernie Formation, Stages of the Jurassic, and ammonite zonations for both northwestern Europe and western North American shown to the left of the stratigraphic column.

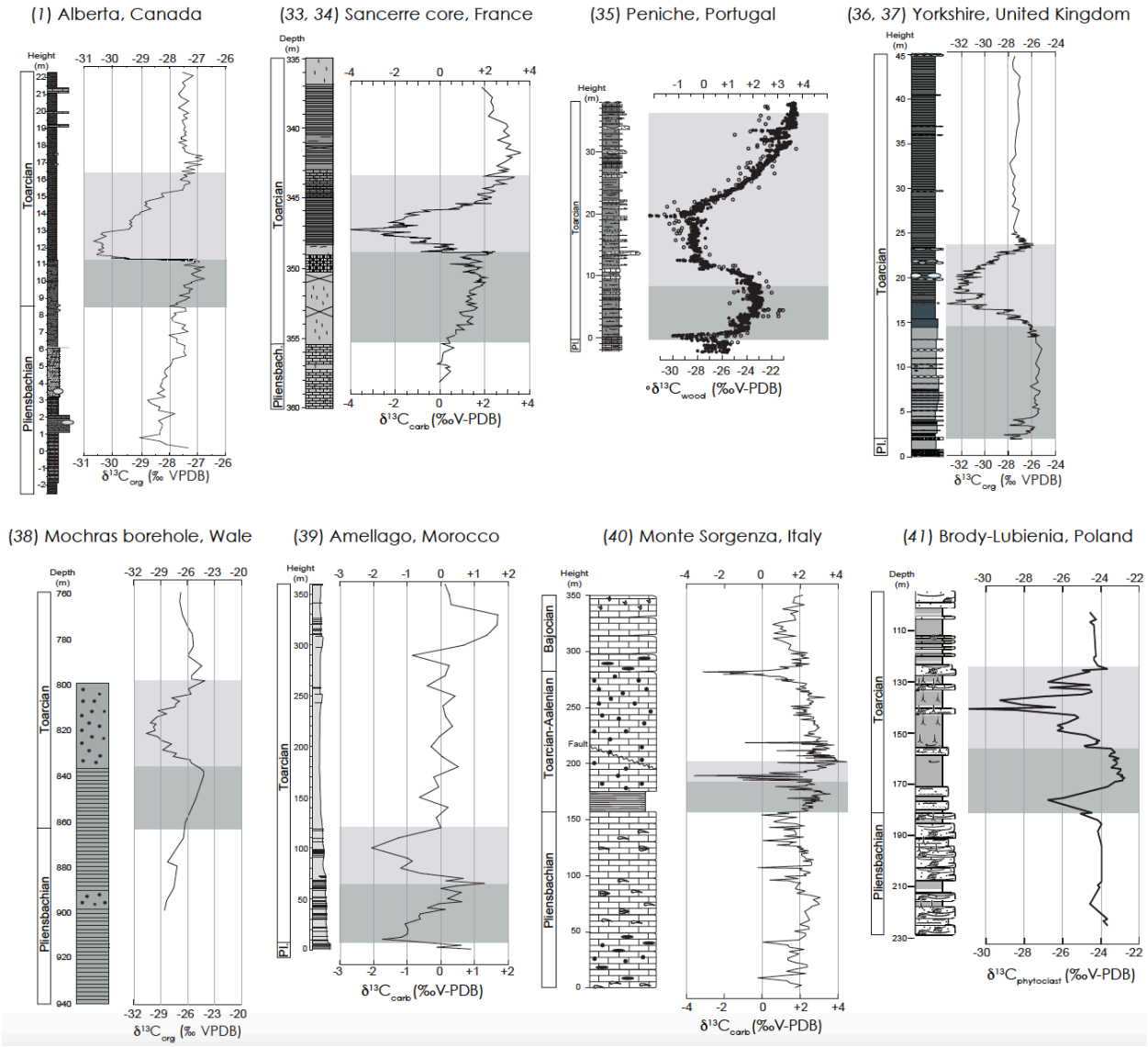

Fig. S3.

Carbon-isotope chemostratigraphies of the Pliensbachian and Toarcian stages from multiple locations. $\delta^{13}C_{org}$ = organic carbon isotopic compositions; $\delta^{13}C_{carb}$ = inorganic carbon isotopic compositions; $\delta^{13}C_{wood}$ and $\delta^{13}C_{phytoclast}$ = organic carbon isotopic compositions of terrestrial plant wood. These carbon-isotope records all display and long-term positive $\delta^{13}C$ trend in the early Toarcian until the pronounced negative CIE associated with the T-OAE (1, 33-39). Dark gray box represents this long-term positive CIE. Light gray box represents the T-OAE CIE. The Tl isotope record suggests that the increased geographical extent of anoxia increased and resulted in the burial of organic carbon (^{13}C-depleted) and ultimately the globally observed trend in higher $\delta^{13}C$ values leading up to the T-OAE.

Additional Data table S1 (separate file)

Iron speciation and thallium isotope data from the East Tributary section.

Additional Data table S2 (separate file)

Carbon isotope, total organic carbon (TOC), iron speciation, and thallium isotope data from drill core 1-35-62-20W5.

Additional Data table S3 (separate file)

Carbon isotope, total organic carbon (TOC), iron speciation, and thallium isotope data from drill core 6-32-75-5W6.

Additional Data table S4 (separate file)

Iron speciation and thallium isotope data from the Dotternhausen section.

924 References

925 1. Them TR II, et al. (2017) High-resolution carbon isotope records of the Toarcian Oceanic
926 Anoxic Event (Early Jurassic) from North America and implications for the global drivers of
927 the Toarcian carbon cycle. *Earth Plan Sci Lett* 459:118–126.
928 2. Them TR, et al. (2017) Evidence for rapid weathering response to climatic warming during the
929 Toarcian Oceanic Anoxic Event. *Sci Rep* 7:5003.
930 3. Röhl H-J, Schmid-Röhl A, Oschmann W, Frimmel A, Schwark L (2001) The Posidonia Shale
931 (Lower Toarcian) of SW-Germany: an oxygen-depleted ecosystem controlled by sea level
932 and palaeoclimate. *Palaeogeo Palaeoclim Palaeoecol* 169:273–299.
933 4. Dickson AJ, et al. (2017) Molybdenum isotope chemostratigraphy and paleoceanography of the
934 Toarcian Oceanic Anoxic Event (Early Jurassic). *Paleocean* 32:813–829.
935 5. Asgar-Deen M, Hall R, Craig RJ, Riediger C (2003) New biostratigraphic data from the Lower
936 Jurassic Fernie Formation in the subsurface of west-central Alberta and their stratigraphic
937 implications. *Can J Earth Sci* 40:45-63.
938 6. Hall RL, Poulton TP, Monger JWH, Field trip A1: Calgary – Vancouver in *Field Guide for the*
939 *Fifth International Symposium on the Jurassic System, Vancouver*, Smith PL, Ed. (Jurassic
940 Sumcomission of the Stratigraphic Commission on the International Union of Geological
941 Sciences, Vancouver, 1998), chap. 2, pp. 29–61.
942 7. Poulton SW, Raiswell R (2002) The low-temperature geochemical cycle of iron: From
943 continental fluxes to marine sediment deposition. *Amer J Sci* 302:774–805.
944 8. Lyons TW, Severmann S (2006) A critical look at iron paleoredox proxies: New insights from
945 modern euxinic marine basins. *Geochim Cosmochim Acta* 70:5698–5722.
946 9. Canfield DE, Poulton SW, Narbonne GM (2007) Late-Neoproterozoic Deep-Ocean
947 Oxygenation and the Rise of Animal Life. *Sci* 315:92–95.
948 10. Poulton SW, Canfield DE (2005) Development of a sequential extraction procedure for iron:
949 implications for iron partitioning in continentally derived particulates. *Chem Geol* 214:209–
950 221.
951 11. Poulton SW, Canfield DE (2011) Ferruginous conditions: A dominant feature of the ocean
952 through Earth's history. *Elem* 7:107–112.
953 12. Berner RA (1984) Sedimentary pyrite formation: An update. *Geochim Cosmochim Acta*
954 48:605–615.
955 13. Raiswell R, Newton R, Wignall PB (2001) An Indicator of Water-Column Anoxia: Resolution
956 of Biofacies Variations in the Kimmeridge Clay (Upper Jurassic, U.K.). *J Sed Res* 71:286–
957 294.
958 14. März C, Poulton SW, Beckmann B, Küster K, Wagner T, Kasten S (2008) Redox sensitivity
959 of P cycling during marine black shale formation: Dynamics of sulfidic and anoxic, non-
960 sulfidic bottom waters. *Geochim Cosmochim Acta* 72:3703–3717.
961 15. Poulton SW, et al. (2015) A continental-weathering control on orbitally driven redox-nutrient
962 cycling during Cretaceous Oceanic Anoxic Event 2. *Geol* 43:963–966.
963 16. Stookey LL (1970) Ferrozine – A New Spectrophotometric Reagent for Iron. *Analy. Chem.*
964 42:779–781.
965 17. Sperling EP, Halverson GP, Knoll AH, Macdonald FA, Johnston DT (2013) A basin redox
966 transect at the dawn of animal life. *Earth Plan Sci Lett* 371-372:143–155.
967 18. Canfield DE, Raiswell R, JWestrich JT, Reaves CM, Berner RA (1986) The use of chromium
968 reduction in the analysis of reduced inorganic sulfur in sediments and shales. *Chem Geol*
969 54:149–155.

19. Aller RC, Mackin JE, Cox RT, Jr (1986) Diagenesis of Fe and S in Amazon inner shelf muds: apparent dominance of Fe reduction and implications for the genesis of ironstones. *Cont Shelf Res* 6:263–289.
20. Rue EL, Smith GJ, Cutter GA, Bruland KW (1997) The response of trace element redox couples to suboxic conditions in the water column. *Deep Sea Res Part I: Ocean Res Pap* 44:113–134.
21. Owens JD, Nielsen SG, Horner TJ, Ostrander CM, Peterson LC (2017) Thallium-isotopic compositions of euxinic sediments as a proxy for global manganese-oxide burial. *Geochim Cosmochim Acta* 213:291–307.
22. Ostrander CM, Owens JD, Nielsen SG (2017) Constraining the rate of oceanic deoxygenation leading up to a Cretaceous Oceanic Anoxic Event (OAE-2: ~94 Ma). *Sci Adv* 3:e1701020.
23. Rehkämper M, Halliday AN (1999) The precise measurement of Tl isotopic compositions by MC-ICPMS: Application to the analysis of geological materials and meteorites. *Geochim Cosmochim Acta* 63:935–944.
24. Nielsen SG, Rehkämper M, Baker J, Halliday AN (2004) The precise and accurate determination of thallium isotope compositions and concentrations for water samples by MC-ICPMS. *Chem Geol* 204:109–124.
25. Baker RGA, Rehkämper M, Hinkley TM, Nielsen SG, Toutain JP (2009) Investigation of thallium fluxes from subaerial volcanism – Implications for the present and past mass balance of thallium in the oceans. *Chem Geol* 73:6340–6359.
27. Caruthers AH, Smith PL (2012) Pliensbachian ammonoids from the Talkeetna Mountains (Peninsular Terrane) of Southern Alaska. *Rev de Paléo Gen* 11:365–378.
28. Caruthers AH, Gröcke DR, Smith PL (2011) The significance of an Early Jurassic (Toarcian) carbon-isotope excursion in Haida Gwaii (Queen Charlotte Islands), British Columbia, Canada. *Earth Plan Sci Lett* 307:19–26.
29. Caruthers AH, Smith PL, Gröcke DR (2013) The Pliensbachian-Toarcian (Early Jurassic) extinction, a global multi-phased event. *Palaeogeo Palaeoclim Palaeoecol* 386:104–118.
30. Percival LME, et al. (2016) Osmium isotope evidence for two pulses of increased continental weathering linked to Early Jurassic volcanism and climate change. *Geol* 44:759–762.
31. Sell B, et al. (2014) Evaluating the temporal link between the Karoo LIP and climatic—biologic events of the Toarcian Stage with high-precision U-Pb geochronology. *Earth Plan Sci Lett* 408:48–56.
32. Ruhl M, et al. (2016) Astronomical constraints on the duration of the Early Jurassic Pliensbachian Stage and global climate fluctuations. *Earth Plan Sci Lett* 455:149–165.
33. Hermoso M, Le Callonnec L, Minoletti F, Renard M, Hesselbo SP (2009) Expression of the Early Toarcian negative carbon-isotope excursion in separated carbonate microfractions (Jurassic, Paris Basin). *Earth Plan Sci Lett* 277:194–203.
34. Hermoso M, et al. (2012) Dynamics of a stepped carbon-isotope excursion: Ultra high-resolution study of Early Toarcian environmental change. *Earth Plan Sci Lett* 319-320:45–54.
35. Hesselbo SP, Jenkyns HC, Duarte LV, Oliveira LCV (2007) Carbon-isotope record of the Early Jurassic (Toarcian) Oceanic Anoxic Event from fossil wood and marine carbonate (Lusitanian Basin, Portugal). *Earth Plan Sci Lett* 253:455–470.
36. Kemp DB, Coe AL, Cohen AS, Schwark L (2005) Astronomical pacing of methane release in the Early Jurassic period. *Nature* 437:396–399.
37. Littler K, Hesselbo SP, Jenkyns HC (2011) A carbon-isotope perturbation at the

1016 Pliensbachian-Toarcian boundary: evidence from the Lias Group, NE England. *Geol Mag*
1017 147:181–192.
1018 38. Jenkyns HC, Gröcke DR, Hesselbo SP (2001) Nitrogen isotope evidence for water mass
1019 denitrification during the early Toarcian (Jurassic) oceanic anoxic event. *Paleocean* 16:593–
1020 603.
1021 39. Bodin S, et al. (2010) Toarcian carbon isotope shifts and nutrient changes from the Northern
1022 margin of Gondwana (High Atlas, Morocco, Jurassic): Palaeoenvironmental implications,
1023 *Palaeogeo Palaeoclim Palaeoecol* 297:377–390.
1024 40. Woodfine RG, Jenkyns HC, Sarti M, Baroncini F, Violante C (2008) The response of two
1025 Tethyan carbonate platforms to the early Toarcian (Jurassic) oceanic anoxic event:
1026 environmental change and differential subsidence. *Sediment* 55:1011–1028.
1027 41. Hesselbo SP, Pieńkowski G (2011) Stepwise atmospheric carbon-isotope excursion during
1028 the Toarcian Oceanic Anoxic Event (Early Jurassic, Polish Basin). *Earth Plan Sci Lett*
1029 301:365–372.
1030 42. Nielsen SG, et al. (2011) Thallium isotopes in early diagenetic pyrite – A paleoredox proxy?
1031 *Geochim Cosmochim Acta* 75:6690–6704.
1032 43. McArthur JM, Algeo TJ, vd Schootbrugge B, Li Q, Howarth RJ (2008) Basinal restriction,
1033 black shales, Re-Os dating, and the Early Toarcian (Jurassic) oceanic anoxic event.
1034 *Paleocean* 23:PA4217.